

Confocal Microscopy

Fatima A. Merchant
*Advanced Digital Imaging
 Research*

Keith A. Bartels
*Southwest Research
 Institute*

**Alan C. Bovik and
 Kenneth R. Diller**
*The University of Texas at
 Austin*

1	Introduction.....	1291
2	Image Formation in Confocal Microscopy	1291
2.1	Lateral Resolution • 2.2 Depth Resolution and Optical Sectioning	
3	Confocal Fluorescence Microscopy	1295
4	Further Considerations.....	1295
5	Types of Confocal Microscopes.....	1295
5.1	Scanning Confocal Microscope • 5.2 The Tandem Scanning Optical Microscope	
6	Limitations of Confocal Microscopy	1296
6.1	Two-Photon Laser Scanning Confocal Microscopy	
7	Biologic Applications of Confocal Microscopy	1298
7.1	Quantitative Analysis of 3D Confocal Microscope Images • 7.2 Cells and Tissues •	
7.3	Microvascular Networks	
8	Conclusion	1308
	References.....	1308

1 Introduction

Confocal microscopes have been built and used in research laboratories since the early 1980s and have been commercially available for only the last few years. The concept of the confocal microscope, however, is almost 50 years old. In 1957, Marvin Minsky [1] applied for a patent on the confocal idea. At that time, Minsky demonstrated great insight into the power of the confocal microscope. He realized that the design of the confocal microscope would give increased resolution and increased depth discrimination ability over conventional microscopes. Independently, in Czechoslovakia, M. Petráň and M. Hadraovsky [2] developed the idea for the tandem scanning optical microscope (a form of the confocal microscope) in the mid-1960s. However it was not until the 1980s, that the confocal microscope became a useful tool in the scientific community. At the time the confocal scope was introduced, the electron microscope was receiving a great deal of attention as it was becoming commercially available. Meanwhile, the confocal microscope required a very high intensity light source, and thus its commercialization was delayed until the emergence of affordable lasers in the technological market. Finally, without the aid of high-speed data processing equipment and large computer memories, taking advantage of the three-dimensional (3D) capabilities of

the confocal microscope was not practical. Visualization of the data was also not feasible without high-powered computers and advanced computer graphics techniques.

Since the early 1980s, research and application of confocal microscopy has grown substantially. A great deal of research has now been done in understanding the imaging properties of the confocal microscope. Moreover, confocal microscopes of different varieties are now commercially available from several quality manufacturers.

2 Image Formation in Confocal Microscopy

There are several different designs of the confocal microscope. Each of these designs is based on the same underlying physical principles. First, these underlying principles will be discussed, and then some of the specific designs will be briefly described.

The confocal microscope has three important features that make it advantageous over a conventional light microscope. First, the lateral resolution can be as great as one and a half times that of a conventional microscope. Second, and most importantly, the confocal microscope has the ability to remove out-of-focus information and thus produce an image of a very

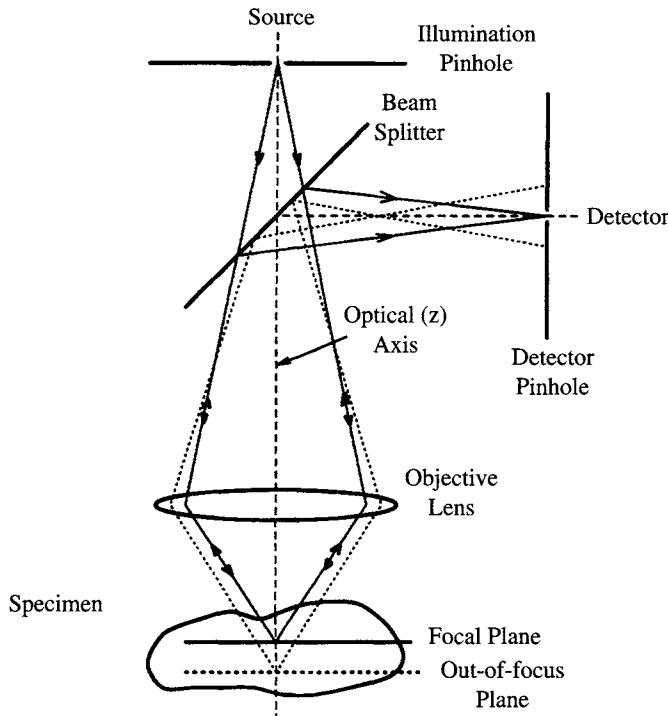


FIGURE 1 Diagram of a confocal microscope. The dashed lines represent light rays from an out-of-focus plane within the specimen; these rays are blocked by the imaging pinhole and do not reach the detector.

thin “section” of a specimen. Third, because of the absence of out-of-focus information, much higher contrast images are obtained.

A schematic representation of a reflectance (dark field) or fluorescence type confocal microscope is shown in Fig. 1. The illumination pinhole produces a point source from which the light ray originates. The ray passes through the beam splitter and down to the objective lens, where it is focused to a point spot inside of the specimen on the focal plane. If the ray reflects off a point in the focal plane, it will take the same path back up through the objective and pass, via the beam splitter, through the imaging pinhole and to the detector. If the ray instead reflects off a point that is out of the focal plane, the ray will take a new path back through the objective lens and will be blocked by the imaging pinhole from reaching the detector. From this simple explanation it is seen that only the focal plane is imaged. This analysis was purely in terms of geometric optics. However, since the resolution of a high-quality microscope is diffraction limited, a diffraction analysis is needed to compare the resolutions of the conventional and the confocal microscope.

2.1 Lateral Resolution

First the lateral resolution of the microscope will be considered. The lateral resolution refers to the resolution in the focal plane of the microscope. The point spread function

(PSF) of a circular converging lens is well known to be the Airy disk [3]. The Airy disk is defined in terms of $J_1(v)$, the Bessel function of order 1. The PSF is defined as the square of the modulus of the amplitude point spread function, $h(v)$, which has the form

$$h(v) = \left[\frac{2J_1(v)}{v} \right] \quad (1)$$

The independent variable v , known as the optical distance, is defined in terms of r , the radial distance from the optical axis in the focal plane:

$$v = \frac{2\pi}{\lambda} \left(\frac{a}{f} \right) r \quad (2)$$

where a is the radius of the lens, λ is the wavelength of the light, and f is the focal length of the lens.

Light is most often detected on an intensity basis. Sheppard and Wilson [4] give the following formulas for calculating the distribution of intensity, $I(x,y)$, for the coherent conventional microscope, the incoherent conventional microscope, and the confocal microscope in terms of the amplitude point spread function. A *coherent microscope* is a microscope in which the illumination source is coherent light. Likewise, an *incoherent microscope* has an incoherent illumination source. Letting $t(x,y)$ be the object *amplitude* transmittance, for the conventional coherent microscope the intensity is

$$I_{cc} = |t * h|^2, \quad (3)$$

for the conventional incoherent microscope the intensity is

$$I_{ci} = |t|^2 * |h|^2, \quad (4)$$

and for the confocal microscope the intensity is

$$I_c = |t * h^2|^2. \quad (5)$$

From a quick examination of these equations, it may not be obvious that the resolution of the confocal microscope is superior. The responses of each type of microscope to a point object are $I_{cc} = |h|^2$, $I_{ci} = |h|^2$, and $I_c = |h|^4$. These responses, with h as defined in Eq. (1), are plotted in one dimension in Fig. 2. In both cases of the conventional microscope, the PSFs are identical and equal to the Airy disk. The confocal PSF is equal to the square of the Airy disk and hence is substantially narrower and has very weak side-lobes. Because of the different imaging properties of the microscopes, the width of the PSF is not a sufficient means by which to describe resolution. Using the width of the PSF, one might conclude that the coherent and incoherent

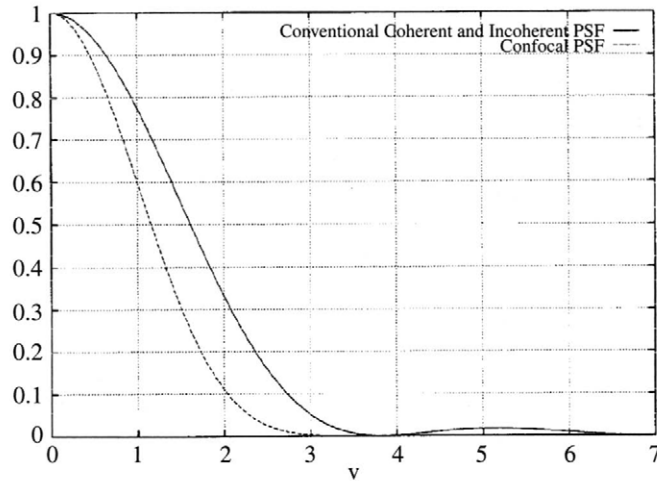


FIGURE 2 Plots of the PSFs for the conventional coherent and incoherent microscopes ($|h|^2$), and the confocal microscope ($|h|^4$).

conventional microscopes have the same resolution. This, as is shown below, is not the case. The resolution of the incoherent microscope is in fact greater than that of the coherent microscope.

The resolution of an optical system is often given in terms of its *two-point resolution*. The two-point resolution is defined

as the closest distance between two point objects such that each object can just be resolved. This is a somewhat loose definition, since one must explain what is meant by *just resolved*. The Rayleigh criterion is often used to define the two-point resolution. The Rayleigh criterion (somewhat arbitrarily) states that the two points are just resolved when the center of the Airy disk generated by one point coincides with the first zero of the Airy disk generated by the second point. The Rayleigh distances for the coherent and incoherent conventional microscope are given in [3] as $0.77 \lambda/\text{N.A.}$ and $0.6 \lambda/\text{N.A.}$, respectively, where N.A. represents the numeric aperture of the objective lens. The numeric aperture is computed as $n \sin \theta$, where n is the index of refraction of the immersion medium and θ is the half-angle of the cone of light that exits the objective. For the confocal microscope, the Rayleigh distance is given in [5] as $0.56 \lambda/\text{N.A.}$.

Figure 3 shows the one-dimensional response to two point objects separated by the Rayleigh distance for the conventional incoherent microscope. The point objects are shown with reduced amplitude on the plot for reference purposes. From Fig. 3, it is evident that the conventional coherent microscope cannot resolve the two point objects. The two points appear as a single large point. The superior resolution of the confocal microscope is demonstrated from this simulation.

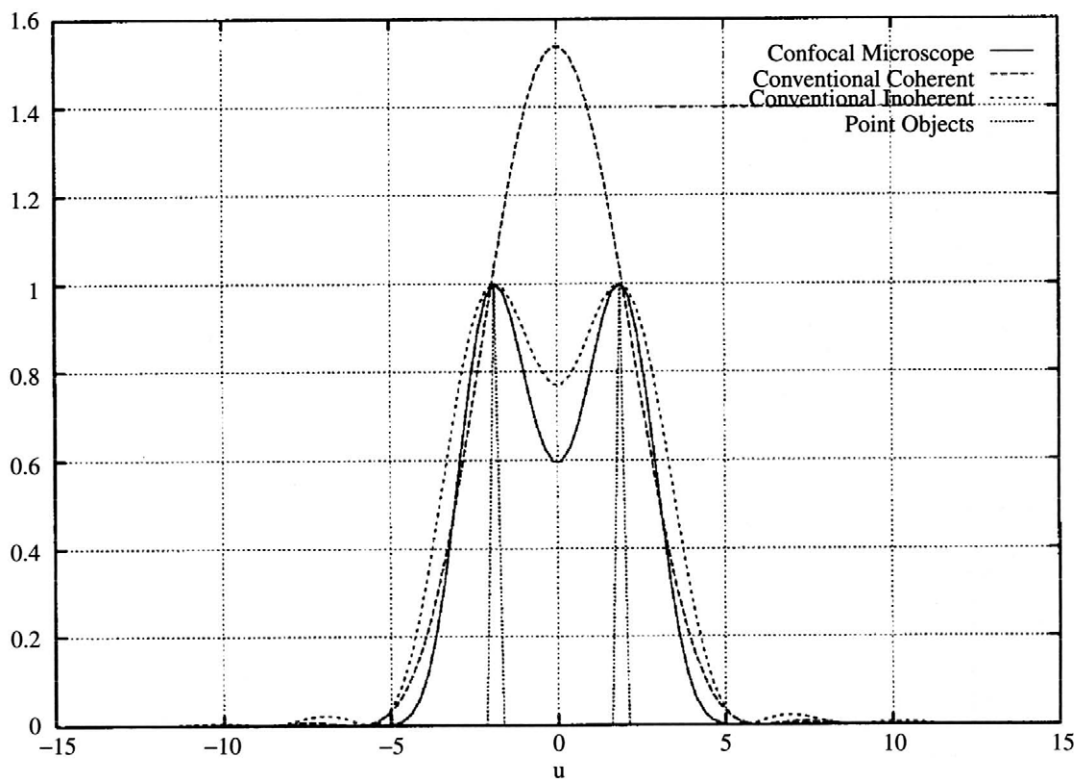


FIGURE 3 Two-point response of the coherent conventional, incoherent conventional, and confocal microscopes. The object points are spaced apart by one Rayleigh distance of the conventional incoherent system.

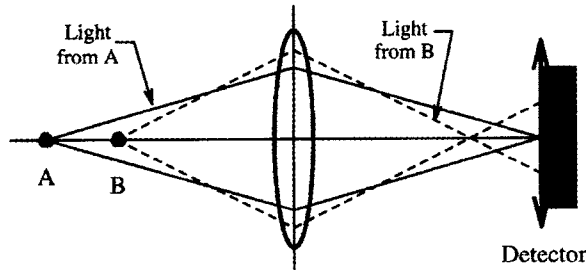


FIGURE 4 In the conventional microscope, the detector output for an in-focus and an out-of-focus point is the same.

2.2 Depth Resolution and Optical Sectioning

The confocal microscope's most important property is its ability to discriminate depth. It is easy to show by the conservation of energy that the conventional microscope has no depth discrimination ability. Consider the conventional detector set up in Fig. 4. The output of the large area detector is the integral of the intensity of the image formed by the lens. When a point object is in focus (at A), the Airy disk is formed on the detector. If the point object is moved out of the focal plane (at B), a pattern of greater spatial extent is formed on the detector (a mathematic description of the out-of-focus PSF is given in [6]). By the conservation of light energy, the integral of these two intensity patterns must be equal and hence the detector output is the same for the in-focus and out-of-focus objects.

In the case of the confocal microscope, the pinhole aperture blocks the light from the extended size of the defocused point

object's image. Early work by Born and Wolf [3] gave a description of the defocused light amplitude along the optical axis of such a lens system. Wilson et al. [5, 6] have adapted this analysis to the confocal microscope. An optical distance along the optical axis of the microscope is defined by

$$u = \frac{8\pi}{\lambda} \sin^2(\alpha/2)z, \quad (6)$$

where z is distance along the optical (z) axis, and $\sin \alpha$ is the numeric aperture of the objective. With this definition, the intensity along the optical axis is given by

$$I_u = \left(\frac{\sin u/2}{u/2} \right)^2 \quad (7)$$

Experimental verification of Eq. (7) has been performed by sectioning through a highly planar mirror [7–9]. Figure 5 shows a plot of $I(u)$ vs. u . The resolution of the z -axis sectioning is most often given as the full width at the half-intensity point. A plot of the z -sectioning width as a function of numeric aperture is given in [7]. A typical example is for an air objective with a N.A. of 0.8, the z -sectioning width is approximately 0.8 μm . For an oil immersion objective with N.A. equal to 1.4, the z -sectioning is approximately 0.25 μm .

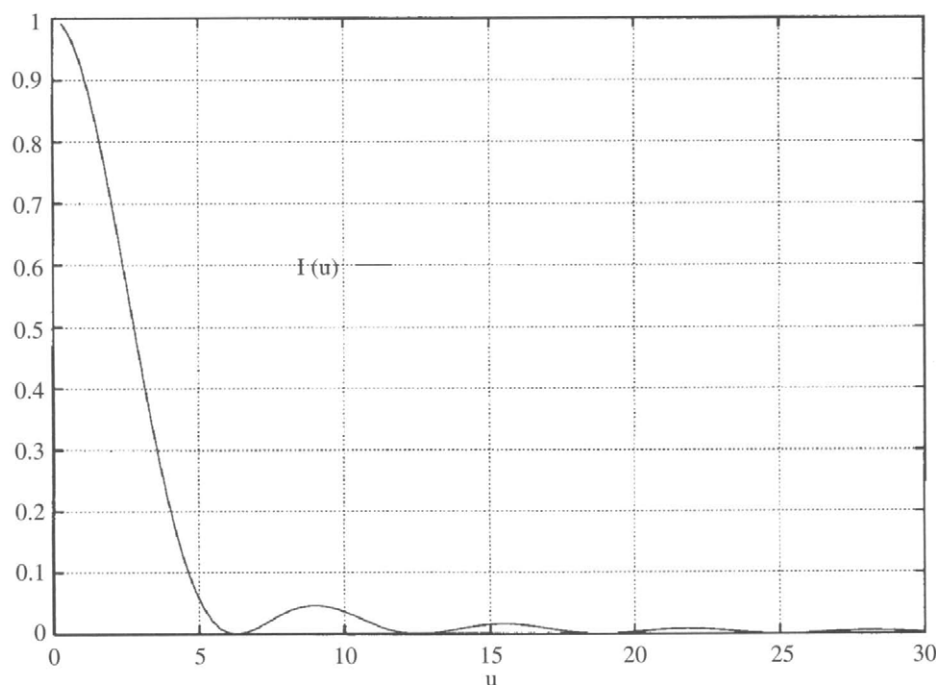


FIGURE 5 Plot of $I(u)$ vs. u , showing the optical sectioning along the optical axis of a confocal microscope.

3 Confocal Fluorescence Microscopy

The analysis presented herein has assumed that the radiation emitted from the specimen is of the same wavelength as the radiation incident on the specimen. This is true for reflectance and transmission confocal microscopy, but not for fluorescence confocal microscopy. In fluorescence confocal microscopy, the image formation no longer takes the form of Eq. (5), but rather of

$$I_c = |t * h(u, v)h(u/\beta, v/\beta)|^2, \quad (8)$$

where β is the ratio of the fluorescent wavelength (λ_2) to the incident wavelength (λ_1), i.e., $\beta = \lambda_2/\lambda_1$, and u and v are rectangular distances in the focal plane. Considering, as before, the case of the circular pupil function

$$I(v) = \left[4 \frac{J_1(v) J_1(v/\beta)}{v - v/\beta} \right]^2 \quad (9)$$

as the lateral PSF in the focal plane. Obviously, if $\beta = 1$ the PSF of the reflection (and transmission) confocal microscope is obtained. As $\beta \rightarrow \infty$, the PSF of the conventional (non-confocal) microscope is obtained. In practice, β will be generally less than 2. A detailed analysis of a confocal microscope in fluorescence mode is given in [7, 10].

4 Further Considerations

In all of the analyses presented here, it is assumed that the pinhole apertures are infinitely small. In practice, the pinhole apertures are of finite radius. In [9], Wilson presents theoretical and experimental results of the effects of various finite pinhole sizes. As one would expect, the resolution in both the axial and transverse directions is degraded by a larger pinhole. Also in [9], Wilson discusses the use of slit, rather than circular, apertures at the detector. The slit detector allows more light to reach the detector than the circular aperture with a compromise of sectioning ability. Wilson has also shown that using an annular rather than a circular lens pupil can increase the resolution of the confocal microscope at the expense of higher sidelobes in the point spread function [5, 7].

5 Types of Confocal Microscopes

Confocal microscopes are categorized into two major types, depending on the instrument design employed to achieve imaging. One type of confocal microscope scans the specimen by either moving the stage or the beam of light, whereas the second type employs both a stationary stage and light source.

5.1 Scanning Confocal Microscope

The scanning confocal microscope is by far the most popular on the market today, and it employs a laser source for specimen scanning. If a laser is not used, then a very high power light source is needed to get sufficient illumination through the source and detector pinhole apertures.

There are two practical methods for the raster scanning of a specimen. One method is to use a mechanical scanning microscope stage. With a scanning stage, the laser beam is kept stationary while the specimen is raster scanned through the beam. The other method is to keep the specimen still and scan the laser in a raster fashion over the specimen. There are, of course, advantages to using either of these scanning methods.

There are two qualities that make scanning the specimen relative to the stationary laser attractive. First, the field of view is not limited by the optics, but by the range of the mechanical scanners. Therefore, very large areas of a specimen can be imaged. A second important advantage of scanning the specimen is that only a very narrow optical path is necessary in the design of the optics. This means that aberrations in the images due to imperfections in the lenses will be less of a problem. A disadvantage of this type of scanning is that image formation is very slow.

The main advantage of scanning the laser instead of the specimen is that the imaging speed is greatly increased. A mobile mirror can be used to scan the laser, in which case an image of 512×512 pixels can be obtained in ~ 1 s. A newer technology of laser scanning confocal microscopes uses acousto-optical deflection devices that can scan out an image at speeds up to TV frame rates. The problem with these acousto-optic scanners is that they are highly nonlinear and special care must be taken in order to obtain distortion-free images.

5.2 The Tandem Scanning Optical Microscope

The tandem scanning optical microscope (TSOM) was patented in Czechoslovakia in the mid-1960s by M. Petráň and M. Hadrovský. The main advantage of the TSOM over the scanning confocal microscope is that images are formed in real time (at video frame rates or greater). Figure 6 shows a simple diagram of the tandem scanning optical microscope. The most important feature of the TSOM is the Nipkow disk. The holes in the Nipkow disk are placed such that when the disk is spun, a sampled scan of the specimen is produced. Referring to Fig. 6, the source light enters a pinhole on the Nipkow disk and is focused onto the specimen through the objective lens. The light reflected off of the specimen goes back up through the objective and up through a corresponding pinhole on the opposite side of the Nipkow disk. The light exiting from the eyepiece can be viewed by the operator, captured on video or digitized, and sent to a computer. In early TSOMs,

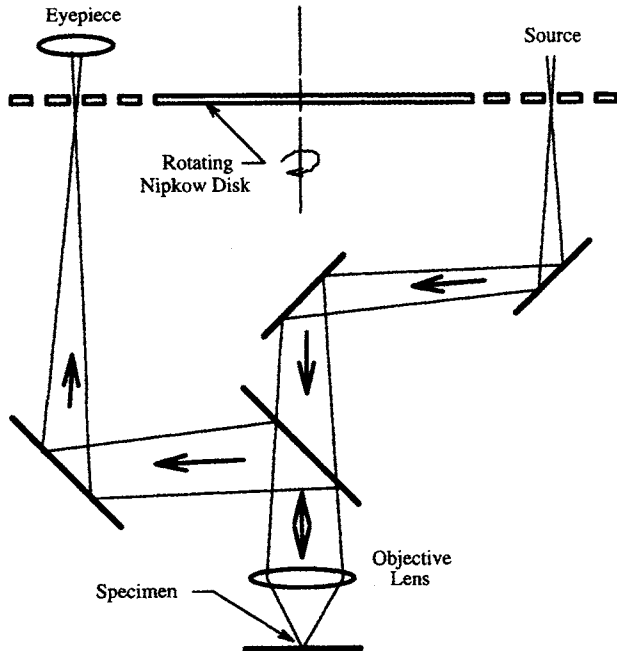


FIGURE 6 Diagram of the tandem scanning optical microscope.

sunlight was used as the illuminating source. Today, though, an arc or filament lamp is generally used. Figure 6 shows the path of a single ray through the system, but it should be noted that several such rays are focused on the specimen at any given instant of time.

Kino et al. [10] altered the above design so that the light enters and exits through the same pinhole. With this design, smaller pinholes can be used since mechanical alignment of the optics is not as difficult. Smaller pinholes, of course, are desirable since the depth of the in-focus plane is directly related to the pinhole size. Kino et al. were able to construct a Nipkow disk with 200,000 pinholes, 20 μm in diameter each, that spun at 2000 RPM. This gave them a frame rate of 700 frames/s with 5000 lines/image.

The TSOM does have certain drawbacks. Because the total area of the pinholes on the Nipkow disk must be negligible (less than 1%) with respect to the total area of the disk [7], the intensity of the light actually reaching the specimen is a very small fraction of that of the source. Depending on the specimen, the amount of light reflected may not be detectable. Another disadvantage of the TSOM is that it is mechanically more complex than the scanning confocal microscopes. Very precise adjustment is needed to keep the tiny pinholes in the rapidly spinning Nipkow disk aligned.

6 Limitations of Confocal Microscopy

In terms of practical applications, although live cell imaging is possible with confocal microscopy, phototoxicity and

photobleaching from repeated exposures to visible light are a major problem. In all microscopes, illumination power is generally constant through all lateral slices of the microscope focus. In confocal fluorescence microscopy, the total one-photon excitation, which depends linearly on the incident illumination intensity is thus constant in each plane throughout the specimen. Confocal microscopy exposes the entire sample to higher-energy photons every time an optical section is generated. Since fluorophores are bleached when excited, photobleaching occurs throughout the thickness of a sample when collecting a series of images. This not only limits the maximum time for image collection, but also limits the amount of time that living tissues can be observed because of the photodamage that occurs due to the production of toxic by-products. In confocal imaging, the one-photon absorption process, which occurs all along the excitation beam, results in phototoxicity and photobleaching throughout the specimen.

6.1 Two-Photon Laser Scanning Confocal Microscopy

Recently, a new optical sectioning technique has been described in which excitation is confined to the optical section being observed by the process of two-photon absorption. Two-photon microscopy is probably the most important development in fluorescence microscopy since the introduction of confocal imaging. Two-photon microscopy is a non-linear process that retains the optical sectioning ability of confocal microscopy, while improving upon its ability to image live cells. Denk and co-workers [11] first introduced the technique of two-photon laser scanning microscopy. The phenomenon of two-photon absorption was discovered by Maria Goppert-Mayer in 1931 [12]. It involves the simultaneous absorption of two photons by a fluorophore. The combined energy of the two photons excites the fluorophore from the ground state to an excited state. The excited state is identical to that caused by a single photon of about half the wavelength. The fluorophore then relaxes back to the ground state, emitting most of the excited energy (approximately twice that of the incident photon) as fluorescence with the same emission wavelength spectrum as is produced in one-photon excitation. Thus, unlike linear fluorescence excitation, the emission wavelength is shorter than the excitation wavelength. Because a fluorophore must absorb two photons per excitation event, fluorescence depends on the square of the incident beam intensity. Moreover, the intensity of the exciting light falls off as $1/z^2$ (z being the distance from the focal plane) above and below focus. Thus, the probability of exciting a fluorophore falls off as $1/z^4$. This non-linear optical absorption behavior limits the excitation to a high-intensity region at the focal point of the focused laser. The extremely high intensities in the focal volume concentrate 80% of the fluorescence generation to the $10^{-10} \mu\text{l}$ focal volume obtained

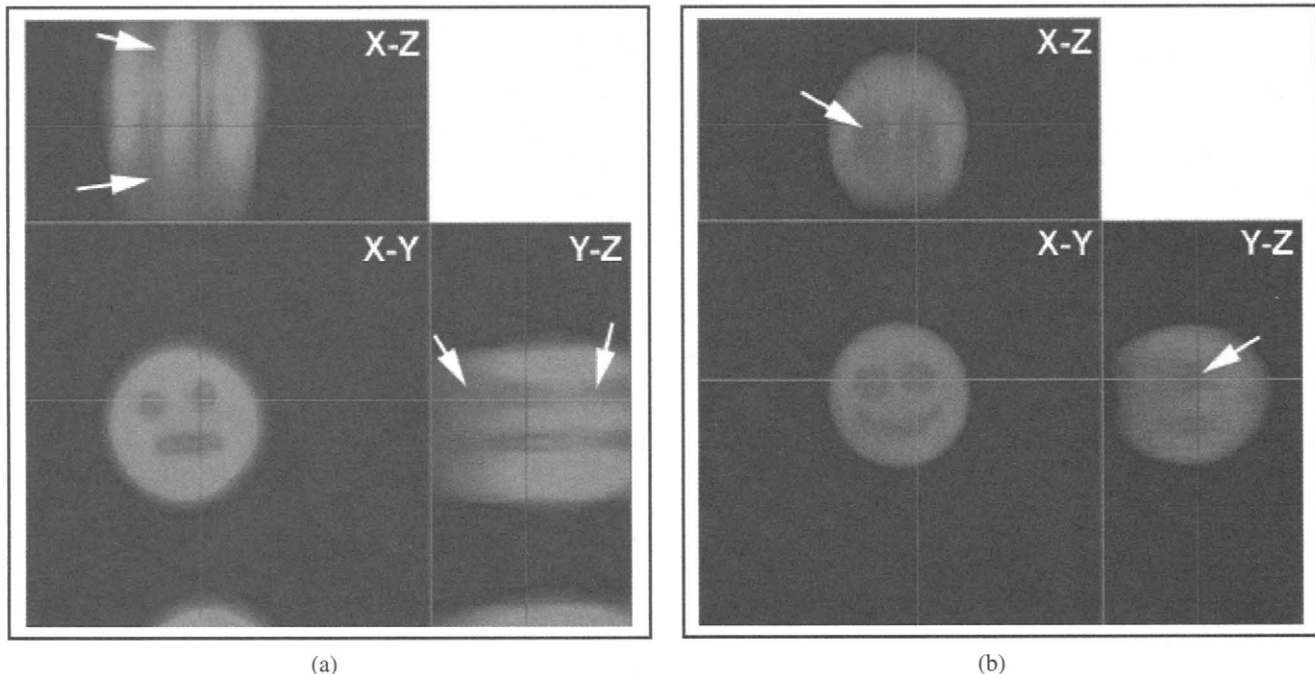


FIGURE 7 Fluorescence excitation in (a) confocal microscopy, and (b) two-photon microscopy. The bleach pattern can be viewed as a footprint of the excitation region. While in confocal microscopy (a), illumination results in excitation throughout the whole thickness of the specimen, the two-photon excitation results in illumination being restricted to the focal plane (b). (See color insert.)

with a high numeric aperture objective [13]. This process thus exhibits unique localization of excitation to the diffraction-limited spot of the focused beam, giving rise to the intrinsic optical sectioning ability of two-photon microscopy. The three-dimensional resolution is due to the confinement of absorption, and consequently excitation, to the focal volume. Therefore, out-of-focus photobleaching and photodamage, and the attenuation of the excitation beam by out-of-focus absorption do not occur. Photodamage at the focal plane does occur, as with the confocal microscopy, but damage above and below the plane of focus is greatly reduced [14]. Two-photon imaging is also useful with ultraviolet (UV) excitable dyes in live cells as the excitation is achieved with infrared light so the cells are never exposed to the more damaging UV excitation. Moreover, the infrared radiation used for excitation in two-photon imaging penetrates into tissue more efficiently than shorter wavelengths, allowing thicker specimens to be imaged.

Figure 7 demonstrates the confinement of excitation to the optical section being observed by the process of two-photon absorption as compared to confocal imaging where the whole thickness of the specimen is excited. Figure 7A shows an optical section (XY) through a green emitting fluorescently labeled polystyrene bead after repeated scanning via confocal microscopy to create a smiley face bleach pattern. This bleach pattern can be viewed as a template of the excitation region. The XZ and YZ sections through the bleaching pattern are also presented to visualize the excitation profile along the axial

plane. Bleaching in this case occurs throughout the sample (indicated by white arrows in the XZ and YZ images), demonstrating that with one-photon excitation, background is excited all along the laser beam. Figure 7B, for comparison, shows an optical section (XY) through a red emitting fluorescently labeled polystyrene bead after repeated scanning via two-photon microscopy to create a smiley face bleach pattern. As seen in the XZ and YZ images, the bleach pattern is confined to the focal plane (indicated by white arrows in the XZ and YZ images). Because the excitation process is limited to the focal spot, out-of-focus photobleaching is greatly reduced. While in confocal microscopy (Fig. 7A), illumination results in excitation throughout the whole thickness of the specimen, the two-photon excitation results in illumination being restricted to the focal plane (Fig. 7B).

The theoretical resolution of two-photon microscopy is typically 1- to 1.3-fold larger than that for conventional fluorescence microscopy, because of the longer wavelength of excitation [13]. The theoretical resolution of confocal microscopy is twice that of two-photon microscopy [15]. When maximum resolution is required, two-photon microscopy is typically coupled with confocal detection (pinhole) [16], or by two-beam interference illumination combined with confocal detection [17].

The imaging process is similar to confocal microscopy. A laser beam is raster-scanned across a focal plane within the labeled specimen, and the emitted fluorescence is detected by a photomultiplier tube to produce a digital image on a

computer. However, since the probability of absorbing two photons depends on the square of the illumination intensity, infrared lasers that compress all of their output into very short ($\sim 10^{-13}$ sec) high energy pulses ($\sim 2\text{kW}$) are needed. It is possible to produce very short, intense light pulses by “mode-locking” a laser light source [18]. The “mode-locked” lasers generate pulses relatively far apart ($\sim 10^{-8}$ sec), so that a peak power in the kilowatt range is reduced to a mean power of a few tens of milliwatts at the specimen (so that the mean power levels are moderate and do not damage the specimen). The laser most commonly employed to date is a tuneable titanium-dopped Sapphire (Ti:Sapphire) laser which operates in the range 690–1000 nm, allowing two-photon excitation of fluorophores normally excited by ultraviolet, blue or green light.

Two-photon fluorescence microscopy has important advantages, particularly in the study of live cells. It has been used to study embryonic development, brain-slice preparations, cellular metabolic activity from NADH autofluorescence, calcium ion activity, and caged bioeffector molecules [19, 20].

7 Biologic Applications of Confocal Microscopy

Confocal microscopy is widely used in a variety of fields including materials science, geology, metrology, forensics, and biology. The enhanced imaging capability of the confocal microscope has resulted in its increased application in the field of biomedical sciences. In general, there is considerable interest in the biologic sciences to study and analyze the 3D structure of cells and tissues. Confocal imaging is a high resolution microscopy technique that provides both fine structural details and 3D information without the need to physically slice the specimen into thin sections. In the area of biologic imaging, confocal microscopy has been extensively used and has led to increase our understanding of the cell’s 3D structure, as well as its physiology and motility.

Recent technical advances have made 3D imaging more accessible to researchers, and the collection of 3D data sets is now routine in several biomedical laboratories. With the dramatic improvements in computing technology, the visualization of 3D data is no longer a daunting task. Several software packages for 3D visualization, both commercial and freeware (<http://www.cs.ubc.ca/spider/ladic/software.html>), are now readily available. These packages include special rendering algorithms that allow (1) the visualization of 3D structures from several viewing angles, (2) the analysis of surface features, (3) the generation of profiles across the surface, and through the 3D volume, and (4) the production of animations, anaglyphs (red-green images) and stereo image pairs. Several books and articles have been written covering the different visualization and reconstruction techniques for

3D data [21–23]. However, little work has yet been done in the quantitative assessment of 3D confocal microscope images. Moreover, the current emphasis in biology is now on engineering quantification and quantitative analysis of information, so that observations can be integrated and their significance understood. Information regarding the topological properties of structure such as the number of objects and their spatial localization per unit volume, or the connectivity of networks cannot be made using single two-dimensional images. Such quantitative measurements have to be made in 3D, using volume data sets. In the following sections, we will present some of the digital image processing methods that may be implemented to obtain quantitative information from 3D confocal microscope images of biologic specimens.

7.1 Quantitative Analysis of 3D Confocal Microscope Images

Three-dimensional data obtained from confocal microscopes is comprised of a series of optical sections, referred to as the “z-series.” The optical sections are obtained at fixed intervals at successively higher or lower focal planes along the z-axis. Each two-dimensional image (2D) is called an “optical slice,” and all the slices together comprise a volume data set. Building up the z-series in depth allows the 3D structure to be reconstructed.

Most of the image processing algorithms for 2D images discussed in the preceding chapters can be easily extended into three dimensions. Quantitative measurements in 3D involve the identification, classification, and tracing of voxels that are connected to each other throughout the volume data set. For the volume data sets, 3D image measurements are generally performed by using two different approaches, either independently, or in conjunction with each other. The first approach involves performing image processing operations on the individual optical sections (2D) of the z-series, and then generating a new (processed) 3D image set to make measurements. The second approach is to perform image processing by using the voxel (volume element), which is the 3D analog of pixel (the unit of brightness in two dimensions). In this case, cubic voxel arrays are employed to perform operations such as kernel multiplication, template matching, and others using the 3D neighborhood of voxels. In either case, quantitative measurements have to be made on the volume data set to determine the 3D relationship of connecting voxels. A summary of the different image processing algorithms for 2D images, which can be applied to the individual slices of a 3D data set without compromising the 3D measurements is discussed by J. Russ in [24]. Certain operations such as skeletonization, however, cannot be applied to single optical slices, and have to be performed in three dimensions, using voxel arrays to maintain the true connectivity of 3D structure. See [25, 26] for a discussion.

In the following sections, we will use examples to demonstrate the application of image processing algorithms to perform quantitative measurements at both the cellular and tissue level in biologic specimens. It will be evident from the examples presented that each volume data set requires a specific set of image processing operations depending on the image parameters to be measured. There are no generic image processing algorithms that can be used to make 3D measurements, so in most cases it is necessary to customize a set of image analysis operations for a particular data set.

7.2 Cells and Tissues

Confocal fluorescence microscopy is increasingly used to study dynamic changes in the physiology of living cell's and tissues, and to determine the spatial relationships between fluorescently labeled features in fixed specimens. Live cell imaging is used to determine cell and tissue viability, and to study dynamic processes such as membrane fusion and fission, calcium-ion fluxes, volumetric transitions, and FRAP (fluorescence recovery after photobleaching). Similarly, immunofluorescence imaging is used determine cellular localization of organelles, cytoskeletal elements, and macromolecules such as proteins, RNA, and DNA. We present examples demonstrating the use of image analysis for confocal microscope images to estimate viability, determine the spatial distribution of cellular components, and to track volume and shape changes in cells and tissues.

7.2.1 Viability Measurements

Fluorescence methods employing fluorescent dyes specifically designed for assaying vital cell functions are now routinely used in biologic research. Propidium iodide (PI) is one such

dye that is highly impermeant to membranes, and it stains only cells that are dead or have injured cell membranes. Similarly, acridine orange (AO) is a weakly basic dye that concentrates in acidic organelles in living plant and animal cells, and is used to assess cell viability. Dead cells are stained red with the PI dye, while the live cells are stained green using AO. Laser scanning confocal microscopy (LSCM) allows the reconstruction of the 3D morphology of both the viable and dead cells. Digital image processing algorithms can then be implemented to obtain an estimate of the proportion of viable and dead cells throughout the cell volume as described below.

Figures 8(a) and 8(b) present series of optical sections that were obtained through an individual islet, at two different excitation wavelengths, 488 nm and 514 nm, for viable and damaged tissue respectively. We implemented image analysis algorithms consisting of template masking, binarization and median filtering (Chapter 2.2) to estimate viability, as described next. The first step involved the processing of each 2D (512×512) image in the sequence of N sections. Template masking was applied to perform object isolation, in which the domain of interest (islet) was separated from the background region. The template mask is a binary image in which the mask area has an intensity of 1 and the background has an intensity of 0. Point wise multiplication of this mask with the individual serial optical sections isolates the islet cross-sections, since the intensity of the background is forced to zero. The advantage of masking, especially in the case of biologic samples, is that the processed images are free of background noise and other extraneous data (i.e., surrounding regions of varying intensity that may occur as a result of the presence of exocrine tissue or impurities in the culture media). The masked images were then binarized using gray-level thresholding operations (discussed in Chapter 2.2).

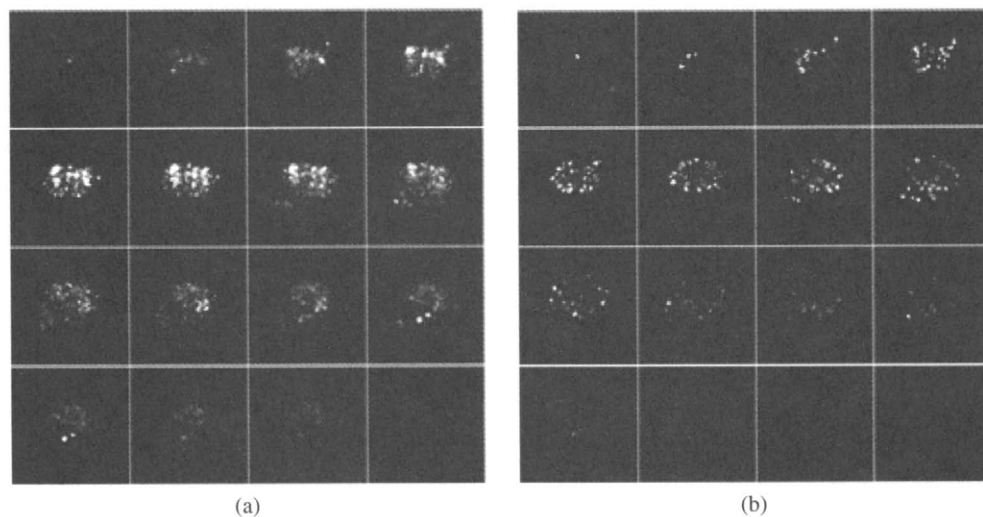


FIGURE 8 Series of 14 optical sections through an islet: (a) viable cells imaged at 488 nm; (b) dead cells imaged at 514 nm (reproduced with permission from [27]).

For 3D (volume) data sets, it is critical to choose a threshold that produces a binary image retaining most of the relevant information for the entire sequence of images. The result of the gray-level thresholding operation is a binary image with each pixel value greater than or equal to the threshold set to 255 and the remaining pixels values set to 0. Binary median filtering was then applied to smooth the binary image. The algorithm to perform median filtering on binary images in the neighborhood (eight-connected) of a pixel counts the incidence of (255 and 0) values of the pixels and its neighbors, determines the majority, and assigns this value to the pixel. The function of median filtering is to smooth the image by eliminating isolated intensity spikes. Following these preprocessing step on each 2D optical section, the 3D data set was then used to determine the total number of fluorescently stained voxels (dead/live) present in the islet. The total number of pixels at an intensity of 255 (indicating the local presence of the fluorescent stain) was recorded for each cross-section of the live and dead cell data sets. The sum of the total pixels for N sections was computed, and the ratio of the sum of the live tissue to that of the dead was determined. This technique was successfully applied to investigate the effect of varying cooling rates on the survival of cryopreserved pancreatic islets [27]. These image processing algorithms can be easily applied to determine the viability in various cells and tissues that have been labeled with vital fluorescent dyes.

7.2.2 Quantification of Spatial Localization and Distribution

In order to take full advantage of the 3D data available by means of confocal microscopy, it is imperative to quantitatively analyze and interpret the volume data sets. An application where such quantification is most beneficial constitutes the spatial localization and distribution of objects within the 3D data set. This is particularly applicable to biologic specimens, because the exact location or distribution of cellular components (e.g., organelles or proteins) within cells is often desired. We will present an example, each for living and fixed cells wherein a 3D quantitative analysis is required, to estimate the distribution of damage within cells, and to determine the cellular localization of a protein, respectively.

Frequently, the elements of interest are represented by either individual voxels (indicating the presence of fluorescently labeled elements) or clusters of connected voxels. It is typically required to determine the location and frequency of occurrence of these objects within the volume data set. There are three steps involved in performing a spatial distribution analysis: (1) identify objects, (2) determine their local position relative to the 3D imaged volume, and (3) determine the frequency of their occurrence within the 3D volume. The first step involves identifying the elements of

interest in the data sets, whose spatial distribution is desired. If individual voxels are to be analyzed, there is no special processing that has to be performed. However, if the objects of interest consist of clusters of connected voxels, an image processing algorithm called *region labeling* or *blob coloring* (Chapter 2.2) is implemented to identify and isolate these objects.

3D Region Labeling. Each image element in 3D is a voxel, and each voxel has 26 neighboring voxels; eight voxels, one at each corner, 12 voxels, one at each edge, and six voxels, one at each surface. A 3D region array may then be defined wherein a similar value (region number/unique color) is assigned for each nonzero voxel in the image depending on its connectivity. The connectivity of a voxel is tested based on a predetermined neighborhood so that all voxels belonging to the same connected region may have the same region number. The size of the neighborhood is chosen depending on image parameters, and the size of the features of interest. Each region or blob is identified by its unique color, and hence the procedure is called blob coloring [28]. For example, the volume data set presented in Fig. 8(b) was analyzed by region labeling to identify and isolate the dead nuclei within the islet volume. The connectivity of voxels was tested using a ten-connected neighborhood. Since the diameter of each nucleus is $\sim 7\text{--}9 \mu\text{m}$ and the serial sectioning was performed at a z-interval of $\sim 2\text{--}5 \mu\text{m}$, it was necessary to use only the six surface voxels and 4 edge voxels for comparison. This decision was made because the use of the voxels at the remaining eight edges and the 12 corners produced artificially connected regions extending from the first to the last section in the 3D image. These artificial regions were larger in size and did not compare with the typical size of a nucleus. An algorithm for 3D blob coloring was implemented, to first scan the data set and check for connectedness so that pixels belonging to the same eight-connected region in the X-Y plane had the same color for each nonzero pixel. The remaining two surface neighbors in the z-direction were then checked for connectedness so that voxels belonging to the same two-connected (voxels in the previous and following z-sections) region had the same color for each non-zero voxel. The final results of this procedure thus contained information on the connectedness of voxels in the 3D image. All voxels belonging to the same ten-connected region were assigned the same color. A threshold was set for the size of each region. Only regions containing more than ten voxels were counted, the rest were assumed to be noise and neglected.

Once the elements of interest [individual voxels/connected voxels (objects)] have been identified, the second step is to determine their spatial location or position within the volume data set. On one hand, for individual voxels, the spatial coordinates along the x, y, and z axes are used to represent position. The position of objects, on the other hand, can be represented in terms of its centroid.

Determination of Centroid. The centroid of an object may be defined as the center of mass of an object of the same shape with constant mass per unit area. The center of mass is in turn defined as that point where all the mass of the object could be concentrated without changing the first moment of the object about any axis [29]. In the 3D case the moments about the X, Y, and Z axes are:

$$\begin{aligned} X_c \iint_I f(x, y, z) dx dy dz &= \iint_I x f(x, y, z) dx dy dz \\ Y_c \iint_I f(x, y, z) dx dy dz &= \iint_I y f(x, y, z) dx dy dz \\ Z_c \iint_I f(x, y, z) dx dy dz &= \iint_I z f(x, y, z) dx dy dz \end{aligned} \quad (10)$$

where (X_c, Y_c, Z_c) is the position of the center of mass. The expressions appearing on the left of these equations are the total mass, with integration over the entire image I . For discrete binary images the integrals become sums, thus the center of mass for 3D binary images can be computed using the following:

$$\begin{aligned} X_c &= \frac{\sum_i \sum_j \sum_k i f(i, j, k)}{\sum_i \sum_j \sum_k f(i, j, k)} \\ Y_c &= \frac{\sum_i \sum_j \sum_k j f(i, j, k)}{\sum_i \sum_j \sum_k f(i, j, k)} \\ Z_c &= \frac{\sum_i \sum_j \sum_k k f(i, j, k)}{\sum_i \sum_j \sum_k f(i, j, k)} \end{aligned} \quad (11)$$

where $f(i, j, k)$ is the value of the 3D binary image (i.e., the intensity) at the point in the i^{th} row, j^{th} column and k^{th} section of the 3D image i.e., at voxel (i, j, k) . Intensities are assumed to be analogous to mass so that zero intensities represented zero mass. The above expressions were used to determine the centroid of the 3D islet volume shown in Fig. 8(b), and the centroid of each damaged nuclei isolated using the region labeling technique. Thus, the spatial position of each damaged nuclei within the islet was determined.

It should be noted here that the position of the individual voxels defined by the (x, y, z) spatial coordinates; or that of objects in terms of the centroid, represent their “global” location with respect to the entire 3D data set. In order to determine the spatial distribution locally, it is necessary to estimate their position relative to some specific feature in the imaged volume. For example, Fig. 8(b) presents a z-series or

volume data set of the damaged nuclei within an islet. The specific feature of interest (or image volume) in this case comprises the islet. The spatial position of the nuclei when expressed only in terms of the centroid then represents their “global” position within the z-series. In order to establish their distribution locally within the imaged islet, it is necessary to determine their location in terms of some feature specific to the islet. Thus, the final stage of a spatial distribution analysis is to determine the frequency and location of the objects with reference to the imaged volume. For cellular structures, this can be accomplished by estimating a 3D surface that encloses the imaged volume. In the islet example, the local distribution of the damaged nuclei can then be described relative to the surface of the islet within which they lie. A technique to estimate the 3D surface of spherical objects is described as follows.

Estimation of 3D Surface. Superquadrics are a family of parametric shapes that are used as primitives for shape representation in computer graphics and computer vision. An advantage of using these geometric modeling primitives is that they allow complex solids and surfaces to be constructed and altered easily from a few interactive parameters. Superquadric solids are based on the parametric forms of quadric surfaces such as the superellipse or superhyperbola, in which each trigonometric function is raised to an exponent. The spherical product of pairs of such curves produces a uniform mathematic representation for the superquadric. This function is referred to as the inside-outside function of the superquadric or the cost function. The cost function represents the surface of the superquadric that divides the 3D space into three distinct regions: inside, outside, and surface boundary.

Model recovery may be implemented by using 3D data points as input. The cost function is defined such that its value depends on the distance of points from the model’s surface and on the overall size of the model. A least-squares minimization method is used to recover model parameters, with initial estimates for minimization obtained from the rough position, orientation, and size of the object. During minimization, all the model parameters are iteratively adjusted to recover the model surface, such that most of the input 3D data points lie close to the surface. To summarize, a superquadric surface is defined by a single analytic function that is differentiable everywhere, and can be used to model a large set of structures like spheres, cylinders, parallelepipeds, and shapes in between. Further, superquadrics with parametric deformations can be implemented to include tapering, bending, and cavity deformation [30].

We will demonstrate the use of superellipsoids to estimate the 3D bounding surface of pancreatic islets. In the example presented, our aim was to approximate a smooth surface to define the shape of islets, and parametric deformations were not implemented. A 3D surface for pancreatic islets

was estimated by formulating a least square minimization of the superquadric cost function with the imaged 3D data points as input [31]. The inside-outside cost function, $F(x, y, z)$, of a superquadric surface is defined by the following equation:

$$F(x, y, z) = \left(\left(\left(\frac{x}{a_1} \right)^{2/\varepsilon_2} + \left(\frac{y}{a_2} \right)^{2/\varepsilon_2} \right)^{\varepsilon_2/\varepsilon_1} + \left(\frac{z}{a_3} \right)^{2/\varepsilon_1} \right)^{\varepsilon_1}, \quad (12)$$

where x , y , and z are the position coordinates in 3D; a_1 , a_2 , a_3 define the superquadric size; ε_1 and ε_2 are the shape parameters.

The input 3D points were initially translated and rotated to the center of the world coordinate system (denoted by the subscript W) and the superquadric cost function in the general position was defined as follows [31]:

$$F(x_W, y_W, z_W) = F(x_W, y_W, z_W : a_1, a_2, a_3, \varepsilon_1, \varepsilon_2, \phi, \theta, \psi, c_1, c_2, c_3) \quad (13)$$

where a_1 , a_2 , a_3 , ε_1 , and ε_2 are described earlier; ϕ , θ , ψ represent orientation; and c_1 , c_2 , c_3 define the position in space of the islet centroid. To recover a 3D surface it was necessary to vary the above 11 parameters to define a set of values such that most of the outermost 3D input data points will lie on or close to the surface. The orientation parameters ϕ , θ , ψ , were neglected in accordance with the rationale of Solina and Bajcsy [30], for the analysis of blob like objects. Only the size and the shape parameters were varied, and the cost function was minimized using the Levenberg-Marquardt method [32]. Further, since multiple sets of parameter values can produce identical shapes, typically certain severe constraints are essential to obtain an unique solution. However, since the recovered 3D surface was used only to represent space occupancy or shape, such ambiguities did not impose a problem [30]. The initial estimates for the size parameters were obtained from the input data points, whereas the shape parameters were initially set to 1. The final parameter values for the 3D surface were determined based on the criterion that the computed surface would enclose $>90\%$ of the 3D input data points. Figure 9 presents a graph of an estimated superquadric surface illustrating the imaged tissue voxels enclosed within or lying on the 3D surface along with the outlying tissue voxels. The estimated surface was then used as a local reference boundary, relative to which the spatial distribution of individual voxels or objects within the islet was determined.

Localization and Distribution. The spatial localization of an element in 3D space can be estimated by describing its position with reference to a morphologic feature, such as an enclosing surface. This information can then be

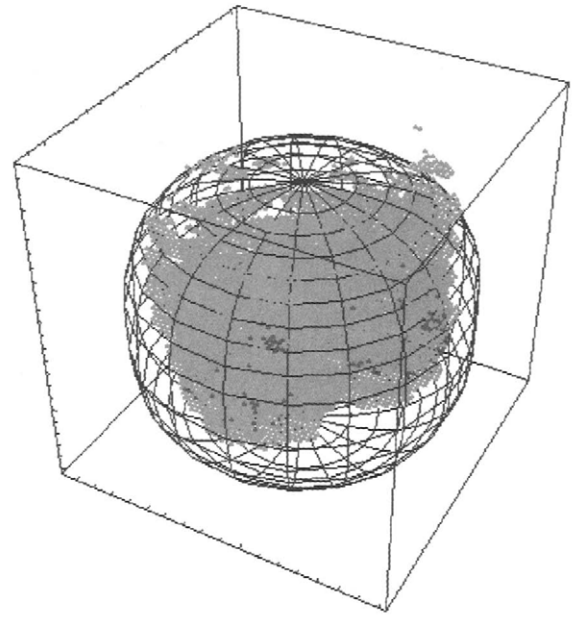


FIGURE 9 Graph of an estimated 3D superquadric surface illustrating the viable (green) and dead (red) tissue voxels enclosed within or lying on the 3D surface along with a few outlying voxels (reproduced with permission from [17]). (See color insert.)

organized into groups to determine the distribution of elements by computing the frequency of elements that occur at similar spatial positions. In the example presented, the 3D spatial distribution of tissue was determined by identifying each voxel (viable and damaged) and computing its relative location in the islet. The spatial location of tissue within the islet was measured by computing the normalized distance of each voxel from the recovered superquadric surface, as described below.

After the surface model was identified, the distance of each viable or damaged image voxel from the centroid of the 3D islet volume was obtained. The distance was then normalized with respect to the length of a vector containing the voxel and extending from the centroid to its intersection with the estimated superquadric 3D surface. Defining the origin O to be fixed at the centroid, and ρ_c to be the length of the vector originating at O , passing through a voxel P , and terminating at the point of intersection with the superquadric surface, S , we then have the coordinates of voxel S as (ρ_c, θ, ϕ) . Voxels P and S have similar θ and ϕ values and different ρ values. Thus, ρ_c is easily obtained from:

$$\rho_c = \sqrt{\left(\left(\left(\frac{\sin \phi \cos \theta}{a_1} \right)^{2/\varepsilon_2} + \left(\frac{\sin \phi \sin \theta}{a_2} \right)^{2/\varepsilon_2} \right)^{\varepsilon_2/\varepsilon_1} + \left(\frac{\cos \phi}{a_3} \right)^{2/\varepsilon_1} \right)^{\varepsilon_1}} \quad (14)$$

where the parameters $a_1, a_2, a_3, \varepsilon_1$, and ε_2 were estimated by means of the nonlinear least-squares minimization of the superquadric cost function.

After ρ_c was obtained, the normalized distance of voxel P from the centroid was computed as ρ/ρ_c . All voxels inside the estimated 3D surface had a normalized distance value less than 1, and surface voxels had a value of 1. Thus the “local” spatial location of each voxel within the islet volume was determined.

For estimating the spatial distribution, each tissue voxel was then assigned to a regional group as a function of its computed normalized distance from the centroid. Thereby 10 serial annular shells were obtained, each having a normalized shell width of 0.1. Thus, the spatial distribution of viable and damaged tissue was computed in the form of a histogram, i.e., the number of voxels were determined for each shell depending upon the normalized distance from the centroid. This technique was used to determine the 3D nature of cryopreservation induced injury in pancreatic islets, and the information was used to obtain a better understanding of the fundamental phenomena underlying the mechanisms of freeze-thaw induced injury [27]. A similar analysis was implemented to determine the spatial distribution of a bacterial protein in mouse fibroblasts cells, fluorescently labeled using indirect immunofluorescence methods [33].

These methods may be easily extended to other applications, biologically oriented or otherwise, to determine the spatial distribution of 3D data.

7.2.3 Dynamic Volumetric Transitions and Shape Analysis

The confocal microscope has the ability to acquire 3D images of an object that is moving or changing shape. A complete volumetric image of an object can be acquired at discrete time instances. By acquiring a sequence of images this way, the time dimension is added to the collected data, and a 4D data set is produced. The addition of the time dimension makes analyses of the data even more difficult, and manual techniques become nearly impossible. Some of the volumetric morphologic techniques described in the previous sections can be easily extended into the time domain. Quantities such as the total volume, surface area, or centroid of an object can be measured over time by simply computing these quantities for each time sample. Simple extensions into the time domain such as this cannot give a detailed picture of how a nonrigid object has changed shape from one time frame to the next. The most difficult analysis is to determine where each portion of an object undergoing nonrigid deformations has moved from one frame to the next.

An overview of a technique that produces detailed localized information on nonrigid object motion is presented. The technique is described in detail in [34, 35]. The technique works by initially defining a material coordinate system for the specimen in the initial frame and computing the

deformations of that coordinate system over time. It assumes that the 3D frames are sampled at a sufficiently fast rate so that displacements are relatively small between image frames.

Let $f_i(x,y,z)$ represent the 3D image sequence in which each 3D frame was sampled at time t_i where i is an integer. The material coordinate system which is “attached” to the object changing shape is given by (u_1, u_2, u_3) . The function that defines the location and deformation of the material coordinate system within the fixed (x,y,z) coordinate system is defined as $\alpha(u_1, u_2, u_3) = (x,y,z)$. To define the position of the material coordinate system at a particular time t_i , the subscript i is added, giving $\alpha_i(u_1, u_2, u_3) = (x_i, y_i, z_i)$. The deformation of the material coordinate system between times t_{i-1} and t_i is given by the function Δ_i , i.e., $\alpha_i = \alpha_{i-1} + \Delta_i$.

The goal of the shape-change technique is to find the functions Δ_i given the original image sequence and the initially defined material coordinates $\alpha_0(u_1, u_2, u_3)$. The functions are found by minimizing the following functional using the calculus of variations [36]:

$$E(\Delta_i) = \lambda P(\Delta_i) + S(\Delta_i), \quad (15)$$

where E is a nonnegative functional that is a measure of the shape-change smoothness, S , and the penalty functional P that measures how much the brightness of each material coordinate changes as a result of a given deformation Δ_i . The parameter λ is a positive real number that weights the tradeoff between the fidelity to the data given by P and the shape-change limit imposed by S . Specifically, the brightness continuity constraint is given by

$$P(\Delta_i) = \int_{u_1} \int_{u_2} \int_{u_3} [f_i(\alpha_{i-1} + \Delta_i) - f_{i-1}(\alpha_{i-1})]^2 du_1 du_2 du_3 \quad (16)$$

The shape-change constraint is given by

$$S(\Delta_i) = \int_{u_1} \int_{u_2} \int_{u_3} (g_i - g_{i-1})^2 du_1 du_2 du_3 \quad (17)$$

where g_i is a 3×3 matrix and function of (u_1, u_2, u_3) called the *first fundamental form* [37] of the material coordinate system. The first fundamental form is a differential geometric property of the coordinate system which completely defines the shape of the coordinate system up to a rigid motion in (x,y,z) space.

The formulation of the shape-change technique is similar to the well-known *optical flow* algorithm presented in [29], except that in this case the smoothness constraint is based on the actual shape of the object rather than simple derivatives of the image. Also, this formulation is presented in three

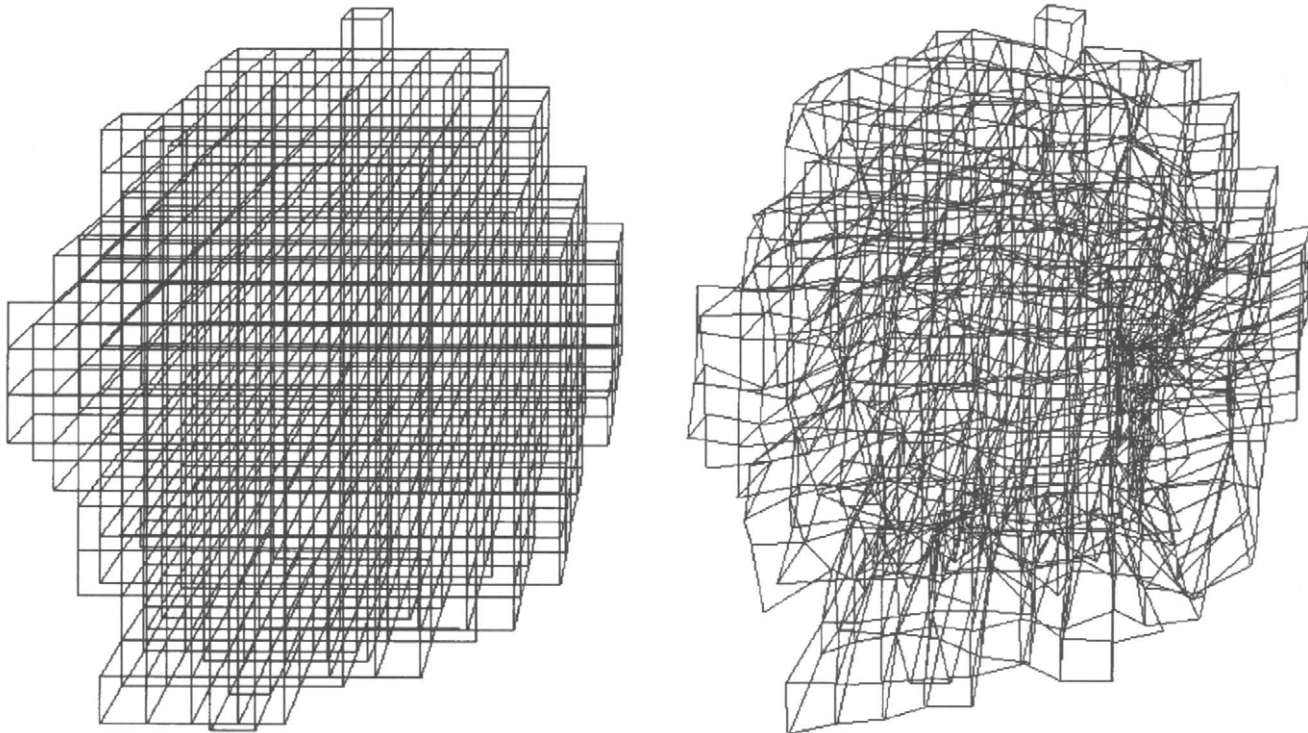


FIGURE 10 Shape-change analysis in a human islet subjected to osmotic stress.

dimensions and produces a model of the shape change for an entire image sequence.

The solution of Eq. (15) requires solution of 3 coupled, nonlinear partial differential equations. A finite difference approach can be used to solve the equations. The resulting solution depends highly on the selection of the parameter λ in Eq. (15). Selection of λ is generally done by trial and error. Once an appropriate value for λ is found, however, it can generally be held constant throughout solution for the entire image sequence. Figure 10 shows the result of running the shape-change algorithm on human pancreatic islets undergoing dynamic volumetric changes in response to osmotic changes due to the presence of a cryoprotective additive (dimethyl sulfoxide) [38].

7.3 Microvascular Networks

Microvascular research is another area in biology that employs various imaging methods to study the dynamics of blood flow, and vascular morphology. One of the problems associated with evaluating microvascular networks relates to the measurement of the tortuous paths followed by blood vessels in thick tissue samples. It is difficult to acquire this information via conventional light/fluorescence microscopy without having to physically section the specimen under investigation. The use of confocal microscopy overcomes this problem by providing in three dimensions, additional spatial

information related to the vascular morphology. However, this now presents the issue of allowing quantitative measurements to be made in the 3D space. In the past, even with 2D data, morphometric evaluation of blood vessel density and diameter has involved manual counting and estimation procedures. There is considerable ambiguity involved in the manual measurement of vessel diameters. Estimating the location of vessel boundaries within the image of microvessels presents a difficult problem. Manual counting of blood vessels is often tedious and time consuming, and the error in measurements typically increases with time. The problem is only compounded in 3D space. Hence, it is necessary to develop computer algorithms to automate the quantitative measurements, thus providing an efficient alternative for measurements of the vascular morphology. We present an example where digital imaging was used to measure the angiogenesis and revascularization processes occurring in rat pancreatic islets transplanted at the renal subcapsular site [39]. Confocal microscopy was employed to image the 3D morphology of the microvasculature, and image processing algorithms were used to analyze the geometry of the neovasculature. Vascular morphology was estimated in terms of 3D vessel lengths, branching angles and diameters, whereas vascular density was measured in terms of vessel to tissue area (2D) and volume (3D) ratios. The image processing algorithms employed are described in the following sections. It should be noted that the methodology described here is suited for microvascular

networks wherein the vessel lengths are perpendicular to the optical axis. For vascular networks, where the vessel direction is parallel to the optical axis so that only vessel cross-sections (circular or elliptical) are known by the 3D image, different image processing algorithms are needed [40].

7.3.1 Data Acquisition and 3D Representation

The revascularization of pancreatic islet grafts transplanted at the renal subcapsular site in rats was evaluated experimentally by means of intravital LSCM of the blood vessels [39]. Three-dimensional imaging of the contrast enhanced microcirculation (5% fluorescein labeled dextran) was performed to obtain serial optical cross-sections through the neovascular bed at defined z-increments. In this example, the acquisition of the optical sections was influenced by curvilinear surface of the kidney. During optical sectioning of the graft microvasculature, images were captured along an inclined plane rather than vertically through the area being sectioned. This occurred as adjacent areas on the surface of the kidney came into focus during optical sectioning. This effect is demonstrated in Fig. 11, which presents the results of a computerized 3D reconstruction performed on 25 optical sections (z-interval of 5 μm) obtained through the vascular bed of an islet graft. As seen in Fig. 11, the curvaceous shape of the kidney is easily distinguished in the 3D reconstruction. Thus, in order to evaluate the 3D vascular morphology, a 2D image was projected from the 3D reconstruction.

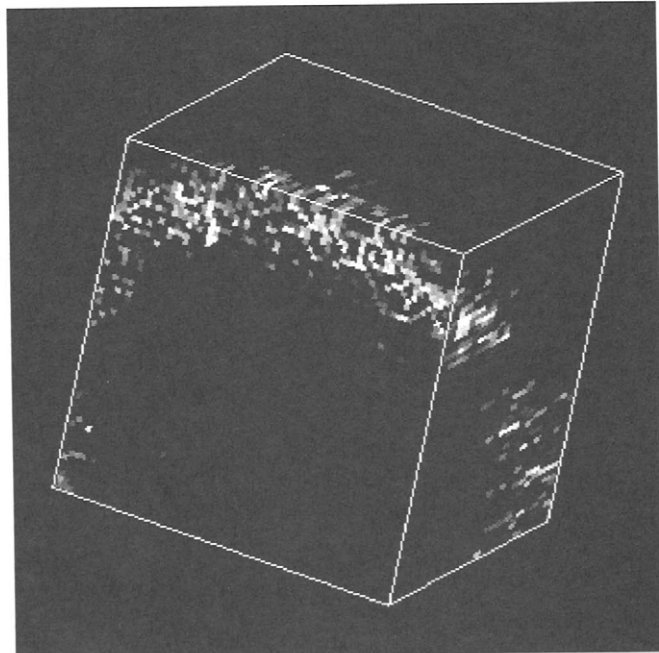


FIGURE 11 Computerized 3D reconstruction performed on 25 optical sections (z interval of 5 μm) obtained through the vascular bed of the kidney. As seen, the curvaceous shape of the kidney is easily distinguished in the 3D reconstruction.

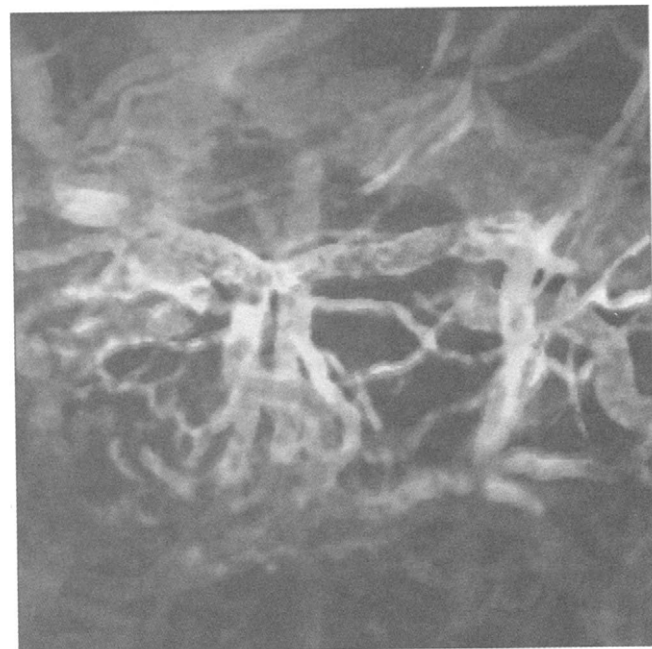


FIGURE 12 3D representation of the microvasculature of an islet graft at the renal subcapsular site. The image is color coded to denote depth. The vessels appearing in the lower portion (blue) are at a depth of 30 μm , whereas those in the middle and upper portions of the image are at a depth of ~ 85 (green) and 135 μm (violet), respectively (reproduced with permission from [39]). (See color insert.)

The composite 2D image representing the 3D morphology was obtained by projection of the individual sections occurring at varying depths (along the z-plane) onto the x-y plane. As shown in Fig. 12, the resulting image consisted of blood vessels that were contiguous in the third dimension. All the morphologic measurements were performed on the composite image.

7.3.2 Determination of Vascular Density

The measurement of the vascular density included a combination of the gray-level thresholding, binarization and median filtering algorithms described in the preceding chapters. Binary images were initially generated via image segmentation using gray-level thresholding. Two-dimensional images of similar spatial resolutions were then smoothed with a 3×3 or 5×5 median filter (Chapter 3.2). The total of the number of pixels at 255 was used as an estimate of the vessel area, and the remaining pixels represented the tissue area. The vessel to tissue area ratios were then computed for each section (areas) or for an entire sequence of sections (volumes).

7.3.3 Determination of Vascular Morphology

Vascular morphology was determined in terms of 3D vessel lengths, vessel diameter, and tortuosity index as described below.

Unbiased Estimation of Vessel Length. Composite images of the projected microvasculature were segmented using gray-level thresholding to extract the blood vessels from the background. The segmented image was then used to obtain a skeleton of the vascular network by means of a thinning operation [41]. The skeletonization algorithm obtains the skeletons from binary images by thinning regions, i.e., by progressively eliminating border pixels that do not break the connectivity of the neighboring (eight-connected) pixels, thus preserving the shape of the original region. The skeletonized image was labeled using the procedure of region labeling and chain coding. The region labeling procedure was implemented with a eight-connected neighborhood for identifying connected pixels. It was used to identify and isolate the different blood vessel skeletons and to determine the length of each segment. Further, the chain coding operation was applied to identify nodes and label vessel segments. The labeled image was scanned to isolate the nodes, by checking for connectivity in the eight-connected neighborhood. Pixels with only one neighbor were assigned as the terminating nodes. Those having greater than two neighbors were classified as junction nodes with two, three or four branches, depending on the connectivity of pixels. The labeled image was pruned to remove isolated short segments without affecting the connectivity of the vascular network. The vessel length was determined as the sum of the total number of pixels in each labeled segment. This approach introduces some systematic bias, because the projection of the 3D data onto a 2D composite results in the lost of some information. An unbiased estimation of the 3D vessel lengths was implemented by applying a modification of the technique described by Gokhale [42] and Cruz-Orive and Howard [43]. This technique eliminated the error introduced in the measurement of the vessel lengths caused by the bias generated during vertical projection of volume data sets.

Gokhale [42] and Cruz-Orive et al. [43] have addressed the issue of estimating the 3D lengths of curves using stereologic techniques. These studies describe a method to obtain an unbiased estimate of the 3D length of linear features from “total vertical projections,” obtained by rotating the curve about a fixed axis and projecting it onto a fixed vertical plane. The length of linear structures is measured for each of the vertical projections. The final estimate of the 3D length is then obtained as the maximum of the different projected lengths. This technique was adapted for our application and implemented as follows. The 3D reconstruction (Fig. 11) was rotated about a fixed axis (y axis) in varying amounts, and the vertical projections were performed to obtain the composite image for each orientation.

The 3D rotations were implemented by means of 3D transformations represented by 3×3 matrices using non-homogenous coordinates. A right-handed 3D coordinate system was implemented. By convention, positive rotations in the right-handed system are such that, when looking from a

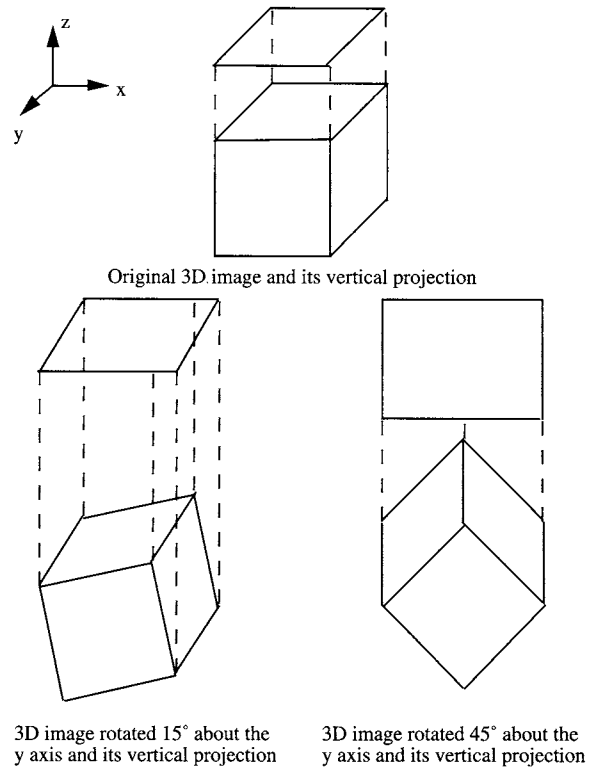


FIGURE 13 3D solid rotated about the y axis and its vertical projections in the x-y plane.

positive axis toward the origin, a 90° counterclockwise rotation transforms one positive axis into another. Thus, for a rotation of the x axis the direction of positive rotation is y to z, for a rotation of the y axis the direction of positive rotation is z to x, and for a rotation of the z axis the direction of positive rotation is x to y. The z axis (optical axis) was fixed as the vertical axis. The y axis was fixed as the axis about which the 3D rotations were performed, and the vertical projections were obtained in the x-y plane. The 3D morphology of the microvascular bed, i.e., the blood vessels, were projected onto the fixed plane (x-y plane) in a systematic set of directions between 0° and 180° , about the y axis as shown in Fig. 13.

The 3×3 matrix representation of the 3D rotation at angle θ about the y axis is

$$R_y(\theta) = \begin{bmatrix} \cos \theta & 0 & -\sin \theta \\ 0 & 1 & 0 \\ -\sin \theta & 0 & \cos \theta \end{bmatrix}. \quad (18)$$

Thus, the geometric transformation of the 3D volume is computed as follows:

$$\begin{bmatrix} x' \\ y' \\ z' \end{bmatrix} = \begin{bmatrix} \cos \theta & 0 & -\sin \theta \\ 0 & 1 & 0 \\ -\sin \theta & 0 & \cos \theta \end{bmatrix} \times \begin{bmatrix} x \\ y \\ z \end{bmatrix}, \quad (19)$$

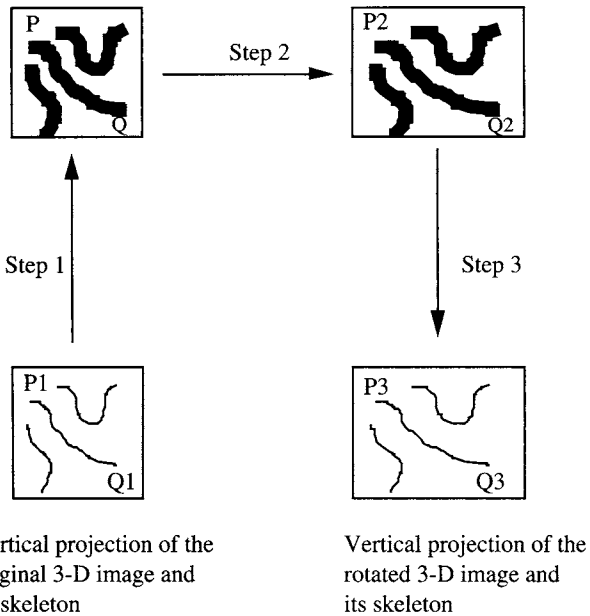


FIGURE 14 Correspondence of vessel segments in the various projected images by means of mapping and 3-D transformations.

where x' , y' , and z' are the transformed co-ordinates, x , y , and z are the original co-ordinates of the reconstructed 3D image, and θ is the angle of rotation about the y axis. The projected length of individual vessel segments may vary in the different projections obtained. Vessel segments were uniquely labeled in each of the composites at different orientations, and the connecting node junctions identified. The unbiased 3D lengths were determined as the maximum of the projected lengths estimated for the various rotations. In order to achieve this, the individual vessel segments at the different rotations have to be matched. The problem involves the registration of each individual vessel segment as it changes in its projected orientation. It was resolved by performing a combination of mapping and inverse mapping transformations. For example, as shown in Fig. 14, an unbiased estimate of the 3D length of segment PQ may be determined as the maximum of the length of the projected segments P1Q1 and P3Q3. It is essential that P1Q1 and P3Q3 are matched as projections of the same vessel segment. This was achieved in three steps. The first step was to match the points P1 and Q1 in the skeletonized image to the points P and Q in the binary image. This was achieved by a simple mapping of points because the skeleton P1Q1 maps onto the centerline of the binary segment PQ. In step 2, the points P and Q were mapped onto the points P2 and Q2 by performing the required transformation to rotate the 3D image. Finally, the binary segment P2Q2 was mapped on to its skeleton P3Q3. Thus a correspondence was established between the two projected lengths P1Q1 and P3Q3. The maximum value of these lengths was a measure of the unbiased length. The tortuosity index was then defined as the ratio of the length of a straight line vector between two

points to the length of the vessel segment between the same points. An index of 1 represents a straight vessel, and < 1.0 represents a curvilinear or tortuous vessel.

Automated Estimation of the Vessel Diameter. In order to automate the vascular diameter measurements, a technique employing linear rotating structuring elements (ROSE) described by Thackray and Nelson [44], was implemented. In this method, various linear structuring elements/ templates of known orientations were constructed to represent shapes frequently occurring in the images [45]. The template was then passed over the labeled image until a match was obtained. At this step, a path was identified through a matched point on the skeleton such that its direction was along the normal to the edge of the vessel (in the image or x - y plane) at the corresponding point in the segmented (binary) image. The diameter was then measured by traversing the two sides from the corresponding point in the segmented image along the defined path until an intensity change occurred from white (255) to black (0). The total distance traversed on both sides was then used as the diameter estimate at that point. The diameter measurements were obtained starting at a point a few pixels (determined as 20% of the total number of pixels in the vessel) from the nodes in order to avoid any erroneous measurements due to the presence of overlapping blood vessels. Further, since each blood vessel segment was labeled individually, the diameter measurements were obtained at various intervals along each segment at points where a template match was found, and the average was determined to obtain an estimate of the vessel diameter along that length.

Determination of Contiguous Vessel Segments. The 3D lengths of the blood vessels were then obtained by identifying all vessel segments that were contiguous in depth. The continuity of vessel segments was determined by two parameters, namely the vessel diameters and the branching and junction angles. The diameters of the various vessel segments meeting at each junction node were examined, and vessel segments having similar diameters and a common junction node were identified as contiguous vessels. Further, at junction nodes of 3 or more vessel segments, the branching angles were measured using the following:

$$\tan \phi_{12} = \left| \frac{m_1 - m_2}{1 + m_1 m_2} \right|, \quad (20)$$

where m_1 and m_2 are the slopes of two vessel segments that are at angle ϕ_{12} to each other.

Two vessel segments were considered to be vessel branches when their junction angle was $< 90^\circ$, and their diameters were different. A vessel segment was identified as a parent vessel if its junction angle with other vessels was $> 90^\circ$. Vessels

segments were identified as crossing or overlapping vessels when their junction angles were $\sim 90^\circ$.

We applied these algorithms to assess and compare the microvasculature of cultured and cryopreserved islets transplanted at the renal subcapsular site in rats [46]. These algorithms may be employed to estimate the morphology of various other vascular networks, including tumor microvasculature, angiograms of patients evaluated for heart disease, and the retinal microvasculature.

8 Conclusion

The past decade has seen a virtual explosion in the application of confocal microscopy to biologic specimens. There is no doubt that the need for quantification of 3D biologic data will steadily grow. Digital image processing can provide numeric data to quantify and substantiate biologic processes. Most often, digital analysis algorithms have to be customized to meet the requirements of the application. We have presented several examples to demonstrate the application of image processing algorithms for analyzing confocal microscope images of biologic specimens. The methodology developed here would be applicable to the general problem of 3D image analysis in both cellular and network structures.

References

- [1] M. Minsky. Microscopy apparatus. United States Patent No. 3,013,467. Filed Nov. 7, 1957; granted Dec. 19, 1961.
- [2] M. Petráň and M. Hadravsky. Method and arrangement for improving the resolving power and contrast. United States Patent No. 3,517,980. Filed Dec. 4, 1967; granted Jun. 30, 1970.
- [3] M. Born and E. Wolf. *Principles of Optics*. Pergamon Press, New York, 1970.
- [4] C. J. R. Sheppard and T. Wilson. Image formation in confocal scanning microscopes. *Optik*, 55:331–342, 1980.
- [5] T. Wilson and C. J. R. Sheppard. *Theory and Practice of Scanning Optical Microscopy*. Academic Press, London, 1984.
- [6] M. Petráň, A. Boyde, and M. Hadravsky. *Confocal Microscopy*, Chapter 9, pp. 245–283. Academic Press, London, 1990.
- [7] T. Wilson, editor. *Confocal Microscopy*. Academic Press, London, 1990.
- [8] G. J. Brackenhoff, H. T. M. Van Der Voort, E. A. Van Spronsen, and N. Nanninga. Three-dimensional imaging by confocal scanning fluorescence microscopy. *Ann. N.Y. Acad. Sci.* 483:405–415, 1986.
- [9] T. Wilson. *The handbook of biological confocal microscopy*, Chapter 11, pp. 99–112. IMR Press, Madison, WI, 1989.
- [10] G. S. Kino and G. Q. Xiao. *Confocal Microscopy*, Chapter 14, pp. 361–387. Academic Press, London, 1990.
- [11] W. Denk, J. H. Strickler, and W. W. Webb, “Two-photon laser scanning fluorescence microscopy,” *Science* 248, pp. 73–76 (1990).
- [12] M. Goppert-Mayer, “Über elementarake mit zwei quantsprungen,” *Ann. Phys.* 9, pp. 273–294 (1931).
- [13] R. M. Williams, D. W. Piston, and W. W. Webb, “Two-photon molecular excitation provides intrinsic 3-dimensional resolution for laser-based microscopy and microphotochemistry,” *FASEB J* 8, pp. 804–813 (1994).
- [14] J. A. Ridsdale and W. W. Webb, “The viability of cultured cells under two-photon laser scanning microscopy,” *Biophys.* 64, pp. A109 (1993).
- [15] M. Gu and C. J. R. Sheppard, “Comparison of 3-dimensional imaging properties between 2-photon and single-photon fluorescence microscopy,” *J Microsc* 177, pp. 128–137 (1995).
- [16] C. J. R. Sheppard and M. Gu, “Image formation in two-photon fluorescence microscopy,” *Optik* 86, pp. 104–106 (1990).
- [17] S. Hell and E. H. K. Stelzer, “Fundamental improvement of resolution with a 4Pi-confocal fluorescence microscope using two photon excitation,” *Optic Commun* 93, pp. 277–282 (1992).
- [18] P. F. Curley, A. I. Ferguson, J. G. White and W. B. Amos, “Application of a femtosecond self-sustaining mode-locked Ti:Sapphire laser to the field of laser scanning confocal microscopy,” *Opt. Quantum Electron.* 24, pp. 851–859 (1992).
- [19] S. M. Potter, “Two photons are better than one,” *Current Biology* 6(12), pp. 1595–1598 (1996).
- [20] P. T. C. So, C. Y. Dong, B. R. Masters and K. M. Berland, “Two-photon excitation fluorescence microscopy,” *Annu. Rev. Biomed. Eng.* 2, pp. 399–428 (2000).
- [21] A. Kriete. *Visualization in Biomedical Microscopies: 3D Imaging and Computer Applications*. VCH publishers, Weinheim, 1992.
- [22] E. M. Johnson, and J. J. Capowski. Principles of reconstruction and 3D display of serial sections using a computer, in *The Microcomputer in Cell and Neurobiology Research* (R. R. Mize, ed.), pp. 249–263. Elsevier, New York, 1985.
- [23] J. K. Stevens, L. R. Mills, and J. E. Trogadis. *Three-Dimensional Confocal Microscopy: Volume Investigation of Biological Systems*. Academic Press, New York, 1994.
- [24] J. C. Russ. *The Image Processing Handbook*, Chapter 10, pp. 589–659. CRC Press, 1994.
- [25] K. J. Halford and K. Preston. 3D skeletonization of elongated solids. *Comput. Vis. Graphics Image Proc.* 27:78–91, 1984.
- [26] S. Lobregt, P. W. Verbeek, and F. C. A. Groen. Three-dimensional skeletonization: principle and algorithm. *IEEE Trans. PAMI* 2:75–77, 1980.
- [27] F. A. Merchant, K. R. Diller, S. J. Aggarwal, and A. C. Bovik. Viability analysis of cryopreserved rat pancreatic islets using laser scanning confocal microscopy. *Cryobiology* 33: 236–252, 1996.
- [28] N. H. Kim, A. B. Wysocki, A. C. Bovik, and K. R. Diller. A microcomputer based vision system for area measurements. *Computat. Biol. Med.* 17:173–183, 1987.
- [29] B. K. P. Horn. Binary Images: Geometric Properties. *Robot Vision*, pp. 46–64. MIT Press, Cambridge, MA, 1986.
- [30] F. Solina and R. Bajcsy. Recovery of parametric models from range images: The case for superquadrics with global deformations. *IEEE Trans. PAMI*. 12:131–147, 1990.
- [31] T. E. Boult, and A. D. Gross. Recovery of superquadrics from depth information. *Proc. Spatial Reasoning Multi-Sensor Fusion Workshop*, 128–137, 1987.
- [32] L. E. Scales. *Introduction to Non-Linear Optimization*. Springer, New York, 1985.

- [33] F. A. Merchant, H. Bayley, and M. Toner. Analysis of spatial and dynamic interaction of an engineered pore forming protein with cell membranes. (In Preparation).
- [34] K. A. Bartels, A. C. Bovik, S. J. Aggarwal, and K. R. Diller. The Analysis of Biological Shape Changes from Multi-Dimensional Dynamic Images. *Journal of Computerized Medical Imaging and Graphics*. 17, 1993.
- [35] K. A. Bartels, C. E. Griffin, and A. C. Bovik. Spatio-Temporal Tracking of Material Shape Change via Multi-Dimensional Splines. *IEEE Workshop on Biomedical Image Analysis*, 1994.
- [36] R. Weinstock, *Calculus of Variations with Applications to Physics and Engineering*. Dover, New York, 1974.
- [37] M. P. Do Carmo. *Differential Geometry of Curves and Surfaces*. Prentice Hall, Englewood Cliffs, NJ, 1976.
- [38] F. A. Merchant, S. J. Aggarwal, K. R. Diller, K. A. Bartels, and A. C. Bovik. Analysis of volumetric changes in rat pancreatic islets under osmotic stress using laser scanning confocal microscopy. *Biomedical Sciences Instrumentation* 29: 111–119, 1993.
- [39] F. A. Merchant, S. J. Aggarwal, K. R. Diller, and A. C. Bovik. In-vivo analysis of angiogenesis and revascularization of transplanted pancreatic islets using confocal microscopy. *Journal of Microscopy* 176:262–275, 1994.
- [40] W. E. Higgins, C. Morice, and E. L. Ritman. Shape based interpolation of tree-like structures in 3D images. *IEEE Trans. Med. Imag.* 12:439–450, 1993.
- [41] T. Pavlidis. A thinning algorithm for discrete binary images. *Comput. Graphics Image Proc.* 13:142–157, 1980.
- [42] A. M. Gokhale. Unbiased estimation of curve length in 3D using vertical slices. *Journal of Microscopy* 159:133–141, 1990.
- [43] L. M. Cruz-Orive and C. V. Howard. Estimating the length of a bounded curve in three dimensions using total vertical projections. *Journal of Microscopy*. 163:101–113, 1990.
- [44] B. D. Thackray and A.C. Nelson. Semi-automatic segmentation of vascular network images using a rotating structuring element (ROSE) with mathematical morphology and dual feature thresholding. *IEEE Transactions on Medical Imaging*. 12:385–392, 1993.
- [45] F. A. Merchant, S. J. Aggarwal, K. R. Diller, and A.C. Bovik. Semi-automatic morphological measurements of 2D and 3D microvascular images. *Proc. IEEE International Conference on Image Processing*. 1:416–420, 1994.
- [46] F. A. Merchant, K. R. Diller, S. J. Aggarwal, and A. C. Bovik. Angiogenesis in cultured and cryopreserved pancreatic islet grafts. *Transplantation* 63:1652–1660, 1997.

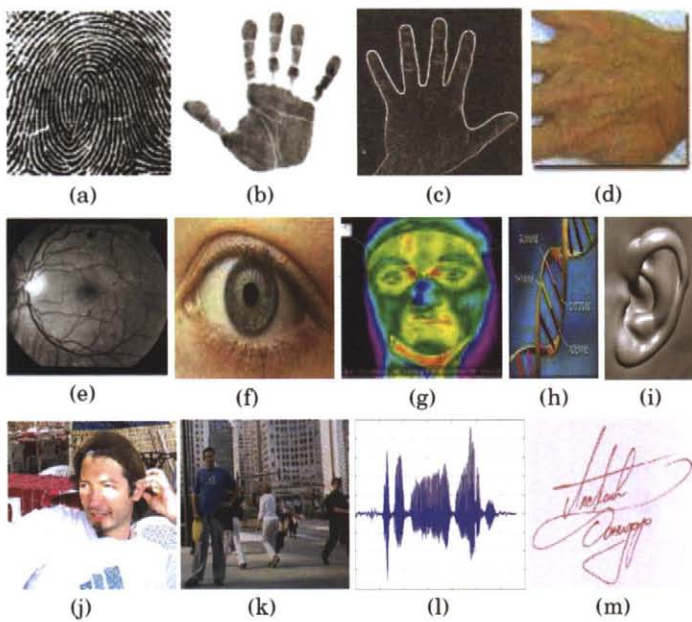


FIGURE 10.8.15 Biometric characteristics: (A) fingerprints; (B) palm print; (C) hand and finger geometry; (D) hand veins; (E) retinal scan; (F) iris; (G) infrared thermogram; (H) DNA; (I) ears; (J) face; (K) gait; (L) speech; (M) signature.

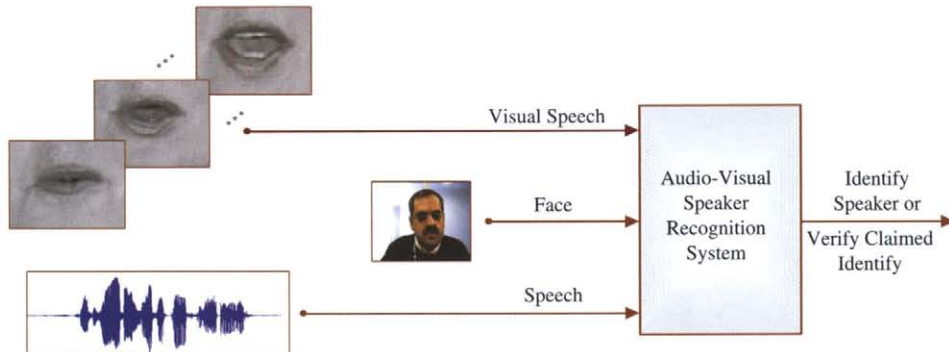


FIGURE 10.8.16 Block diagram of an audiovisual speaker recognition system that utilizes static (face image) and dynamic (visual speech) visual information together with acoustic information.

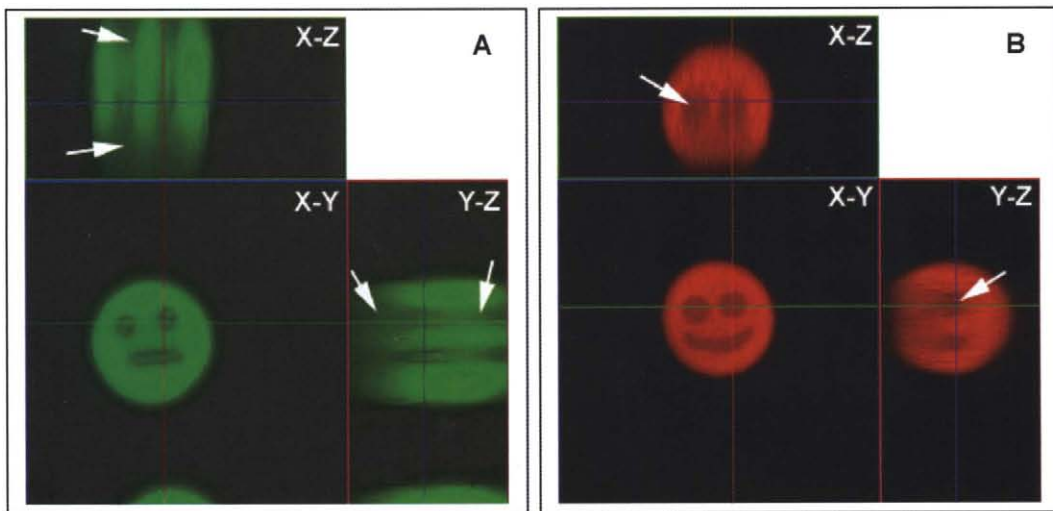


FIGURE 10.9.7 Fluorescence excitation in (a) confocal microscopy, and (b) two-photon microscopy. The bleach pattern can be viewed as a footprint of the excitation region. While in confocal microscopy (a), illumination results in excitation throughout the whole thickness of the specimen, the two-photon excitation results in illumination being restricted to the focal plane (b).

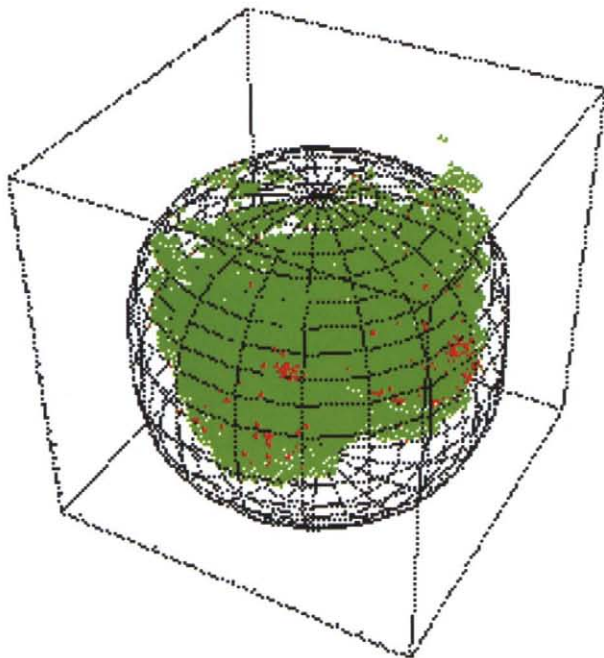


FIGURE 10.9.9 Graph of an estimated 3-D superquadric surface illustrating the viable (green) and dead (red) tissue voxels enclosed within or lying on the 3-D surface along with a few outlying voxels (reproduced with permission from [17]).

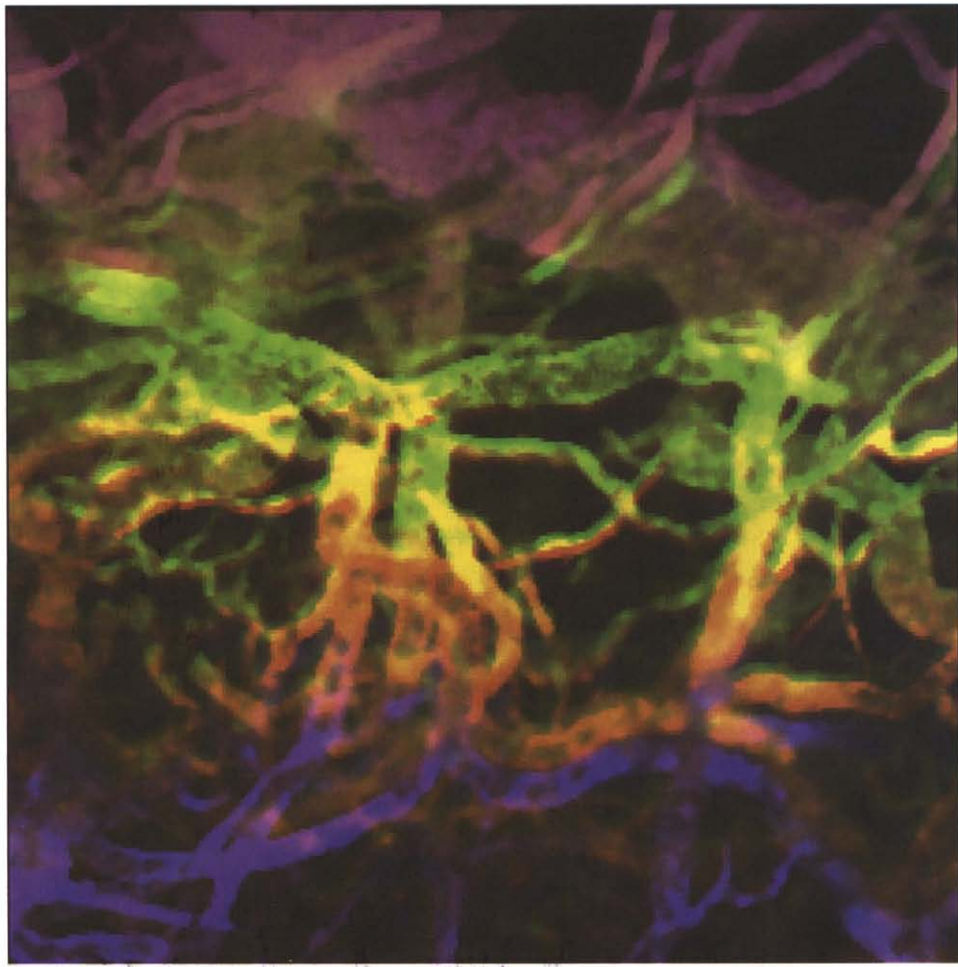


FIGURE 10.9.12 3-D representation of the microvasculature of an islet graft at the renal subcapsular site. The image is color coded to denote depth. The vessels appearing in the lower portion (blue) are at a depth of $30 \mu\text{m}$, whereas those in the middle and upper portions of the image are at a depth of ~ 85 (green) and $135 \mu\text{m}$ (violet), respectively (reproduced with permission from [39]).